RSC Applied Interfaces

ROYAL SOCIETY OF CHEMISTRY

PAPER

View Article Online
View Journal | View Issue



Cite this: *RSC Appl. Interfaces*, 2025, **2**, 1311

# Hollow $SnO_2$ nanosphere-coated separators for dendrite-free lithium metal batteries†

Yi Chen, Xingyan Zeng, Yufei Yang, Xuyang Wang, Hui Nie, * Xingping Zhou and Xiaolin Xie

Received 11th April 2025,
Accepted 28th May 2025

DOI: 10.1039/d5lf00101c

rsc.li/RSCApplInter

Serious dendrite formation remains a significant challenge for the practical application of high-energy lithium metal batteries (LMBs). Fabricating separators with a high lithium ion transference number ($t_{Li^+}$) and uniform pore structure is an effective strategy to homogenize $Li^+$ flux and suppress dendrite growth. Here, hollow $SnO_2$ nanospheres with high structural stability were synthesized through a solvothermal method for surface coating of a poly(ethylene-*co*-acrylic acid) (EAA) separator (EAA@$SnO_2$). The EAA matrix enhances the $t_{Li^+}$ through the interaction of carboxyl groups with ions in the electrolyte, while hollow $SnO_2$ nanospheres convert to $Li_xSn$ during cycling, regulating $Li^+$ flux and promoting uniform solid electrolyte interphase formation. The as-prepared separator-based Li symmetric cells demonstrate stable cycling for over 1000 h with a low overpotential of 17 mV. Additionally, the $LiFePO_4$||Li cells with the EAA@$SnO_2$ separator deliver an initial capacity of 116.6 mA h $g^{-1}$ and a capacity retention of over 80.96% after 200 cycles at 5C. The utilization of metallic hollow $SnO_2$ nanospheres for separator coating proves to be a promising strategy for high-performance LMBs.

## Introduction

Lithium metal batteries (LMBs) are regarded as the "holy grail" of next generation batteries due to its exceptional theoretical capacity of 3860 mA h $g^{-1}$ and the lowest redox potential of −3.04 V.[1,2] Nevertheless, the Li metal reacts with electrolytes during cycling due to its high reactivity, leading to an unstable solid electrolyte interface (SEI) and severe dendrite growth.[3,4] These challenge results in the reduced Coulombic efficiency and poor cycling stability, ultimately impeding the practical application of LMBs.[5,6] Until now, strategies such as modification of anodes,[7–9] electrolyte additives,[10,11] solid-state electrolytes[12–14] and artificial SEIs[15,16] have been developed to address the above issues. Among them, the design of a functional separator presents an effective approach to mitigate the above issues.

The separator in batteries isolates the cathode and anode while allowing the transport of $Li^+$ through its porous structure. Nonpolar polyolefin separators exhibit a non-uniform porous structure, which consequently leads to an inhomogeneous $Li^+$ flux and accelerates the dendrite growth.[17,18] Moreover, according to Sand's time, the cells with those separators with a high lithium ion transference number ($t_{Li^+}$) exhibit a reduced propensity for dendrite formation while the $t_{Li^+}$ of polyolefin separators is only 0.2–0.4.[19,20] Various strategies have been developed to mitigate the issue of dendrite growth. It has been demonstrated that increasing the polarity of separators enhances their interaction with ions in the electrolytes, thereby increasing the $t_{Li^+}$.[21,22] One effective strategy is the modification of polyolefin separators with polar polymers,[23,24] inorganic compounds,[25,26] metal–organic frameworks,[27–29] or covalent organic frameworks.[30,31] Another strategy for suppressing dendrite growth is fabrication of separators using polar polymers, including polyimide (PI),[32,33] polyether ether ketone (PEEK)[34,35] and poly(vinylidene fluoride) (PVDF).[36] In our previous work, the poly(ethylene-*co*-acrylic acid) (EAA) separator has been fabricated by a facile template etching method. The carboxyl groups in the EAA layer of this separator significantly enhance the $t_{Li^+}$ and inhibit the dendrite growth, which has been proved by solid nuclear magnetic resonance spectroscopy and molecular dynamics simulations.[37]

Except increasing $t_{Li^+}$, regulating the $Li^+$ flux is another effective way to promote homogenous $Li^+$ deposition. Metallic materials such as Mg,[38] Au,[39] Cu[40] and Ge[41] have been incorporated into separators to regulate the $Li^+$ flux due to their lithiophilic properties. Among them, Sn is particularly promising due to its similar nucleation overpotential to lithium, which facilitates homogeneous lithium plating/stripping.[42]

*Key Laboratory of Material Chemistry for Energy Conversion and Storage, Ministry of Education, School of Chemistry and Chemical Engineering, Huazhong University of Science and Technology, Wuhan 430074, China. E-mail: huinie@hust.edu.cn*

† Electronic supplementary information (ESI) available: XPS, pore distribution and EDX mapping of $SnO_2$; LSV, CV and EIS of EAA@$SnO_2$ separators; photographs of symmetric cells. See DOI: https://doi.org/10.1039/d5lf00101c

$SnO_2$ has been utilized in separators of Li–S batteries for its adsorption and catalytic abilities.[43–45] In addition, $SnO_2$ converts to lithiophilic $Li_xSn$ alloys with a two-step reaction, which is beneficial for uniform Li deposition.[46,47] However, serious volume expansion (>300%) happens during this process, which hinders their further application.[48]

In this study, hollow $SnO_2$ nanospheres were synthesized and coated on the surface of EAA porous separators, forming EAA@$SnO_2$ composite separators. The incorporation of hollow $SnO_2$ nanospheres to separators facilitates the alloying with lithium, thereby constructing a uniform electric field and forming a smooth SEI. This unique hollow structure provides sufficient space to accommodate the volume expansion of Sn while ensuring a homogeneous $Li^+$ flux. Furthermore, the carboxyl groups on the EAA layer boost the $t_{Li^+}$ of separator to 0.74. The synergistic effect of EAA and $SnO_2$ effectively suppresses dendrite growth, resulting in a dendrite-free anode. Notably, the EAA@$SnO_2$ assembled Li symmetric cell could cycle for over 1000 h at a current density of 0.5 mA $cm^{-2}$ with an overpotential of 17 mV. Impressively, the EAA@$SnO_2$-based $LiFePO_4$ (LFP)||Li cells maintain a capacity retention of over 80.96% at 5C after 200 cycles. Our research indicates that the EAA@$SnO_2$ separator holds significant promise for application in fast-charging LMBs.

# Experimental

### Materials

Ethylene acrylic acid 6100 (EAA 6100) was purchased from SK Chemicals (the content of acrylic acid is 10 wt%). Polyethylene glycol 2000 (PEG 2000), hydrochloric acid (HCl, 36.5–38 wt%), tetrahydrofuran (THF) and ethanol (EtOH) were purchased from Sinopharm Chemical Reagent Co. (Shanghai, China). Tin tetrachloride ($SnCl_4{\cdot}5H_2O$) and polyacrylic acid (PAA) were purchased from Aladdin Biochemical Technology Co., Ltd. (Shanghai, China). The liquid electrolyte of 1 mol $L^{-1}$ $LiPF_6$ in a mixed solvent [V(EC):V(DEC) = 1:1] was purchased from Duoduo Chemical Reagent Network. Polyethylene (PE) was obtained from Jiangsheng Material Co. (Hubei, China).

### Preparation of hollow $SnO_2$ nanospheres

Hollow $SnO_2$ nanospheres were synthesized by a hydrothermal method. 0.38 g $SnCl_4{\cdot}5H_2O$ was dissolved in a mixture of 4 mL deionized water and 40 mL EtOH followed by 1 mL HCl. The solution was stirred for 30 min to obtain a homogeneous solution. After that, the solution was transferred into a Teflon-lined stainless-steel autoclave and heated at 200 °C for 24 h. Then, the solution was cooled to room temperature naturally. The obtained product was washed with deionized water and ethanol several times to remove the impurities and dried at 60 °C overnight.

### Preparation of EAA@$SnO_2$ separators

The preparation of the EAA separator was based on our previously developed fabrication procedures.[37] 0.7 g EAA and 0.5 g PEG 2000 were dissolved in 10 mL THF with magnetic stirring at 65 °C for 1 h. The resulting solution was then cast onto a glass substrate using a 750 μm doctor blade at 60 °C. After standing for 1 min, the substrate was immersed in water to remove the THF and PEG 2000. The EAA separator was then transferred to ethanol and dried at room temperature.

25 mg $SnO_2$ was dispersed in 10 mL EtOH with 2.5 mg PAA as a binder and ultrasonicated for 30 min. After that, the $SnO_2$ dispersion was sprayed onto the EAA separator with a pressure of 0.1 MPa and a distance of 10 cm, and dried naturally to obtain the EAA@$SnO_2$ separator.

### Characterization

Crystallinity of the as-prepared $SnO_2$ was characterized by X-ray powder diffraction (XRD, XRD-7000) analysis with Cu-Kα ($\lambda$ = 1.54178 Å) radiation with $2\theta$ ranging from 20–80° at a scanning rate of 5° $min^{-1}$. The morphology of $SnO_2$ was characterized by transmission electron microscopy (TEM, HT7800), high-resolution transmission electron microscopy (HRTEM, Talos F200X) and scanning electron microscopy (SEM, Hitachi S-4700). The microstructure of the EAA@$SnO_2$ separators was characterized by SEM. The contact angle between the separators and liquid electrolyte was evaluated using a contact angle tester (OCA20).

### Electrochemical measurements

Ionic conductivity was determined by electrochemical impedance spectroscopy (EIS) using an Autolab PGSTAT302N, and calculated *via* the following equation:

$$\sigma = \frac{d}{R_d \times S} \quad (1)$$

where $d$, $R_d$ and $S$ are the thickness of the separator, bulk resistance and the area of the electrode, respectively.

The electrochemical stability was measured from liner sweep voltammetry (LSV) from 0 to 7.0 V at a scan rate of 1 mV $s^{-1}$.

The lithium ion transference number ($t_{Li^+}$) was evaluated by combining chronoamperometry and EIS analysis using Li symmetric cells. $t_{Li^+}$ was calculated according to the following equation:

$$t_{Li^+} = \frac{I_s(\Delta V - I_0R_0)}{I_0(\Delta V - I_sR_s)} \quad (2)$$

where $I_0$ and $I_s$ are the initial current and steady-state current, $R_0$ and $R_s$ are the interfacial resistance before and after polarization, respectively, and $\Delta V$ is the potential difference (10 mV).

The battery performance of the separators was examined by using LFP|separator|Li cells, which was assembled in a glove box. The testing voltage was 2.5 to 3.9 V.

## Results and discussion

The hollow $SnO_2$ nanospheres were synthesized through a solvothermal method. XRD was utilized to characterize the crystal structure and phase purity of the as-synthesized hollow $SnO_2$ nanospheres. As demonstrated in Fig. 1a, its (110), (101), (211) and other diffraction peaks are consistent with the standard XRD patterns of $SnO_2$ (PFD: 00-41-1445) with a tetragonal rutile structure. Moreover, the absence of additional peaks indicates that the hollow $SnO_2$ nanospheres exhibit high phase purity. The hollow $SnO_2$ nanospheres were further characterized by X-ray photoelectron spectroscopy (XPS). As shown in Fig. 1b, two distinct peaks at 495.36 eV and 486.96 eV are observed, corresponding to $SnO_2$ $3d_{3/2}$ and $SnO_2$ $3d_{5/2}$, respectively. These peaks confirm the formation of $Sn^{4+}$, thereby validating the successful formation of $SnO_2$. Additionally, the absence of the Cl 2p peak in the XPS spectrum confirms the complete removal of the Cl element (Fig. S1†). The as-prepared white $SnO_2$ powder consists of uniform nanospheres, as displayed in Fig. 1c. Moreover, a size analysis of 100 hollow $SnO_2$ nanospheres reveals a normal distribution pattern, with an average diameter of 478 nm (Fig. S2†). The morphology of hollow $SnO_2$ nanospheres was further examined by TEM. As shown in Fig. 1d, it is indicated that the $SnO_2$ features a uniform spherical shape, which is consistent with the results from SEM images. Moreover, it could be seen that the edge of nanospheres is darker than the center, suggesting the hollow structure of the $SnO_2$ nanospheres. Moreover, the shell thickness of $SnO_2$ is about 120 nm from the SEM image of the broken $SnO_2$ (Fig. S3†). The distinct lattice fringes observed in the HRTEM image (Fig. 1e) reveal that the lattice spacing of adjacent lattice planes is 0.335 nm, corresponding to the (110) plane of the tetragonal rutile structure of $SnO_2$. Fig. 1f shows the nitrogen adsorption–desorption isotherm of hollow $SnO_2$ nanospheres. The hollow $SnO_2$ nanospheres demonstrate a type-IV adsorption/desorption isotherm at $P/P_0 > 0.4$, accompanied by type H2(b) hysteresis loops within the $P/P_0$ range of 0.45 to 0.98. Furthermore, the specific surface area of $SnO_2$ is measured to be 32.56 $m^2\ g^{-1}$. The pore size distribution presented in Fig. S4† exhibits that the hollow $SnO_2$ nanospheres possess a porous structure with an average pore size of 6.0 nm, attributed to the interstitial spaces between constituent nanoparticles during the assembly of the nanospheres. The $SnO_2$ with a porous structure can absorb more electrolytes, and the increased specific surface area amplifies the availability of active sites, thereby optimizing the interaction with Li.

The EAA separator was prepared based on the previously developed procedure. The slurry with EAA and PEG 2000 in THF was bladed on the glass substrate at 60 °C. After drying for 1 min at 60 °C and then template etching, the original EAA separator was prepared. The EAA@$SnO_2$ separator was fabricated *via* a spraying method using slurry comprising hollow $SnO_2$ nanospheres and PAA in a mass ratio of 10 : 1 (Fig. 2a). The concentration of the hollow $SnO_2$ nanospheres in the slurry was 2.5 mg $mL^{-1}$. As shown in Fig. 2b, the hollow $SnO_2$ nanospheres are distributed uniformly on the

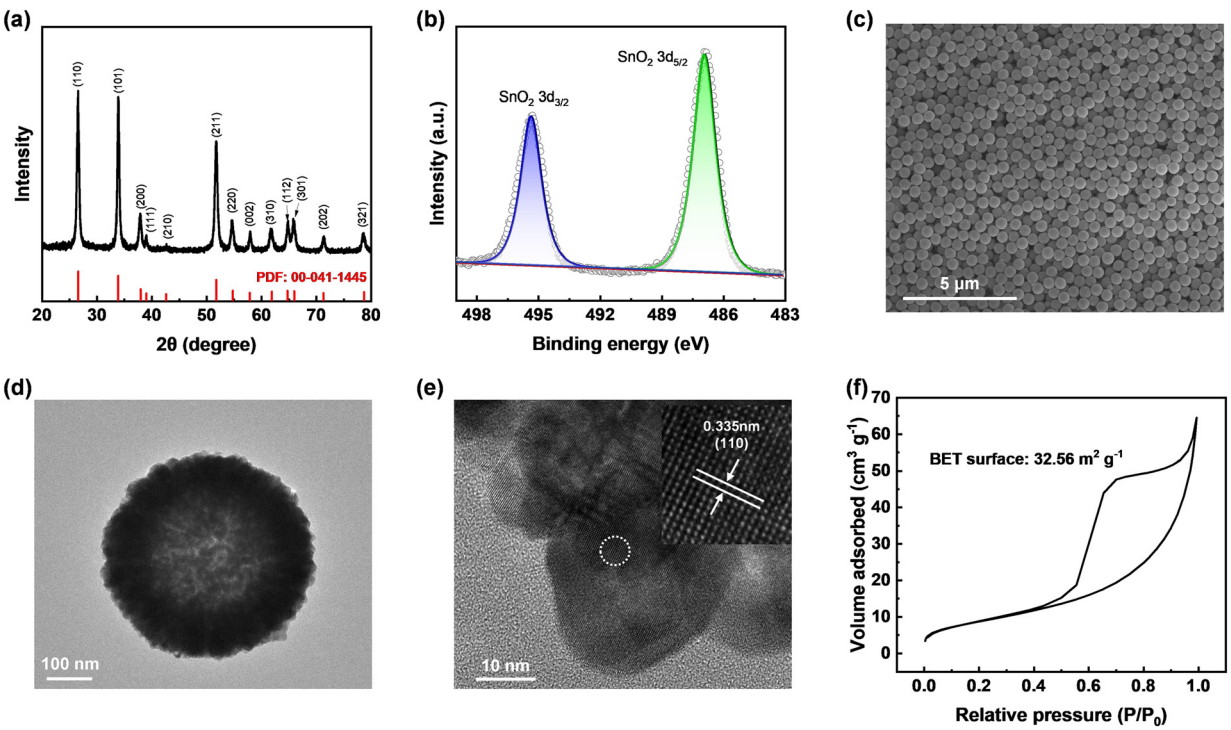


**Fig. 1** Characterization of hollow $SnO_2$ nanospheres. (a) XRD pattern (standard card: PFD: 00-41-1445); (b) XPS spectrum of Sn 3d; (c) SEM image; (d) TEM image; (e) HRTEM image; (f) nitrogen adsorption–desorption isotherm.

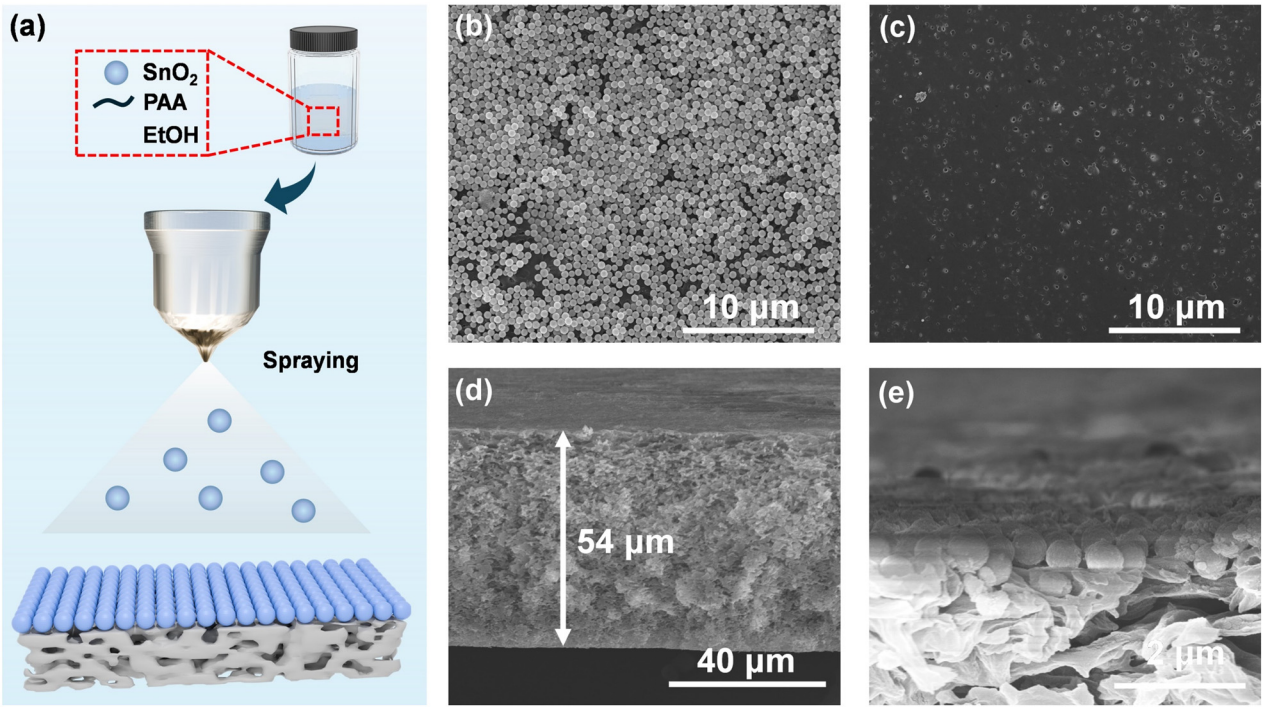


Fig. 2 (a) Fabrication process of EAA@$SnO_2$ separators. SEM images of the (b) coating side and (c) uncoated EAA side of EAA@$SnO_2$ separators. (d) Cross-section and (e) the enlarged cross-section SEM images of EAA@$SnO_2$ separators.

surface of EAA. Moreover, the uncoated side shows the porous morphology of the EAA matrix (Fig. 2c). The cross-section SEM image illustrates that the thickness of the EAA@$SnO_2$ separator is 54 μm, with the $SnO_2$ layer being so thin that it is nearly invisible (Fig. 2d). Moreover, the enlarged cross-sectional SEM image shown in Fig. 2e demonstrates that the $SnO_2$ fits tightly on the EAA separator with about 1 layer of hollow $SnO_2$ nanospheres on the surface. Correspondingly, this suggests that the thickness of the distinct $SnO_2$ coating layer is about 400–600 nm with a weight of 1.41 mg $cm^{-2}$.

The introduction of inorganic nanoparticles enhances the physical properties of the EAA@$SnO_2$ separators. As illustrated in Fig. 3a and S5,† the contact angle of the EAA@$SnO_2$ separator is 34°, which is lower than those of PE (45°) and EAA (41°). The carboxyl groups on EAA enhance the polarity of the polyolefin backbone, thereby improving its wettability with electrolytes. Additionally, the superior wettability of hollow $SnO_2$ nanospheres further reduces the contact angle of the separator with the electrolyte, enabling a better interaction between the electrode and electrolyte. Consequently, the electrolyte uptake of the separator exhibits a trend analogous to that of the contact angle. Due to the high porosity of the EAA separator, its electrolyte uptake is 111.2%, higher than that of PE (92.2%). Furthermore, the incorporation of hollow $SnO_2$ nanospheres, with their hollow structure and interstitial gaps, enhances electrolyte uptake, resulting in an electrolyte uptake of 122.6% for the EAA@$SnO_2$ separator. The thermal stability of EAA@$SnO_2$ was evaluated by thermogravimetric analysis (TGA). As displayed in Fig. S6,† EAA@$SnO_2$ remains thermally stable up to 400 °C, with 5.20% of the residual mass attributed to $SnO_2$. Li||stainless steel (SS) cells, equipped with different separators, were assembled to evaluate the electrochemical stability of separators through LSV analysis. As shown in Fig. 3b, all the separators are electrochemically stable at a voltage of $U$ = 2.5–4.0 V, which is consistent with the operational voltage window of LMBs. Moreover, as displayed in Fig. 3c, the SS||SS cells were further assembled to estimate the ionic conductivity of separators through EIS measurements. Due to the increased thickness of EAA and EAA@$SnO_2$ separators, their bulk resistances are higher than that of PE. However, the ionic conductivity of the EAA@$SnO_2$ separator reaches 0.56 mS $cm^{-1}$, which is the highest among these separators. This enhanced performance can be attributed to the improved electrolyte uptake and the lithiophilicity of $SnO_2$. Similarly, the $t_{Li^+}$ of the EAA@$SnO_2$ separator increases as well. As illustrated in Fig. 3d and e and S7,† the $t_{Li^+}$ of the EAA@$SnO_2$ separator reaches 0.74, which is higher than that of the EAA separator. In addition to the anchoring effect of carboxyl groups on EAA towards $PF_6^-$, hollow $SnO_2$ nanospheres play a crucial role in facilitating the transport of $Li^+$. The narrow pores in hollow $SnO_2$ nanospheres selectively allow $Li^+$ to pass through while permitting the diffusion of $PF_6^-$ and solvents. Moreover, the $Li_xSn$ alloys formed through electrochemical reactions exhibit superior lithiophilicity, facilitating the rapid transport of $Li^+$. Consequently, based on Sand's time, the improved $t_{Li^+}$ of the EAA@$SnO_2$ separators is expected to exhibit the most effective dendrite inhibition compared with EAA and PE

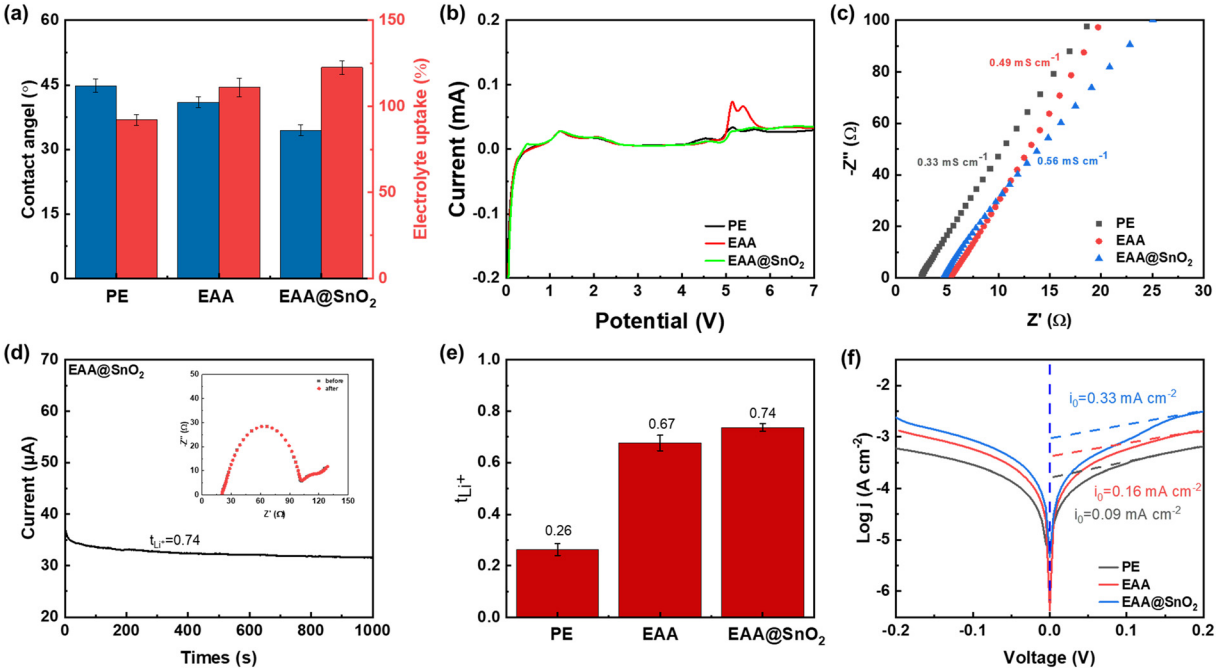


**Fig. 3** (a) The contact angles of various separators with electrolytes. (b) The LSV curves of PE, EAA and EAA@$SnO_2$ separators, respectively. (c) The EIS spectra of PE, EAA and EAA@$SnO_2$ separators, respectively. (d) Chronoamperometry profile of the EAA@$SnO_2$ separator. The inset is the EIS spectra before and after polarization. (e) The $t_{Li^+}$ of PE, EAA and EAA@$SnO_2$ separators, respectively. (f) The Tafel plots from Li||Li cells with PE, EAA and EAA@$SnO_2$ separators, respectively.

separators. The charge-transfer kinetics are further enhanced by the presence of $SnO_2$. As displayed in Fig. 3f, the exchange current density ($j_0$) of the EAA@$SnO_2$ separator is 0.33 mA $cm^{-2}$, twice that of EAA separators. It is attributed to the high lithiophilicity of $SnO_2$, which promotes the $Li^+$ deposition.

Li||Li symmetric cells were assembled with PE, EAA and EAA@$SnO_2$ separators to investigate the Li plating/stripping behaviours. The cells were filled with a carbonate-based electrolyte (1 M $LiPF_6$ in EC : DEC = 1 : 1 vol/vol) and tested at a current density of 0.5 mA $cm^{-2}$ and 1 mA h $cm^{-2}$. As shown in Fig.4a, the cell with the PE separator exhibits stable cycling for over 300 h, after which an increase in voltage is observed, ultimately leading to failure after 400 h. The Li|EAA|Li and Li|EAA@$SnO_2$|Li cells demonstrate a stable cycling for over 1000 hours, attributed to their enhanced $t_{Li^+}$, which effectively suppresses dendrite growth. Notably, the voltage hysteresis of the EAA@$SnO_2$-based cell is as low as 17 mV, whereas that of EAA-based cells is 25 mV. This improvement can be attributed to the lithiophilicity of $SnO_2$, which facilitates the formation of $Li_xSn$ alloys ($0 \le x \le 4.4$) upon $Li^+$ intercalation. The $Li_xSn$ alloys exhibit enhanced electron conductivity, thereby mitigating the voltage hysteresis observed in the EAA@$SnO_2$-based cells. The morphology of Li anodes in Li|EAA@$SnO_2$|Li cells after 100 h cycling at 0.5 mA $cm^{-2}$ was analysed to investigate the impact of hollow $SnO_2$ nanospheres on the electrode morphology. As shown in Fig. 4b, the electrode in contact with the EAA side of the EAA@$SnO_2$ separator demonstrates a uniform Li deposition, although some minor holes are observed. In contrast, the electrode facing the $SnO_2$ side displays a smooth, defect-free SEI (Fig. 4c). It is because that $SnO_2$ undergoes a reaction with $Li^+$ to initiate the formation of Sn, which subsequently reacts to generate $Li_xSn$ alloys through the above two-step process. These alloys facilitate the $Li^+$ flux and promote the formation of a uniform SEI. Moreover, as illustrated in Fig. 4d, the hollow $SnO_2$ nanospheres maintain their structures after cycling, indicating that the hollow structure of $SnO_2$ effectively prevents the volume expansion, showing no negative effect on the regulation of the $Li^+$ flux. Besides, $LiPF_6$ is uniformly distributed across the EAA@$SnO_2$ separator especially in the regions containing hollow $SnO_2$ nanospheres from the EDX mapping (Fig. S8†). *In situ* Li symmetric cells were further studied to observe the Li deposition behaviour. As shown in Fig. S9,† the PE separator-assembled cell exhibits loose Li deposition with significant and uncontrollable dendrite formation within 600 s at a high current of 3 mA. In contrast, the Li deposition of cells using EAA separators is denser, though some dendrites are still present. Notably, the Li|EAA@$SnO_2$|Li cell shows a dense and uniform lithium deposition with minimal dendrite formation, indicating enhanced suppression of lithium dendrites (Fig. 4e). The inherent lithiophilicity of $SnO_2$ promotes the formation of $Li_xSn$ alloys and enhances electron transport within the SEI, contributing to a more uniform and stable SEI layer.

The LFP||Li cells with various separators were assembled to evaluate the electrochemical performance of the EAA@$SnO_2$ separators. Cyclic voltammetry (CV) was utilized

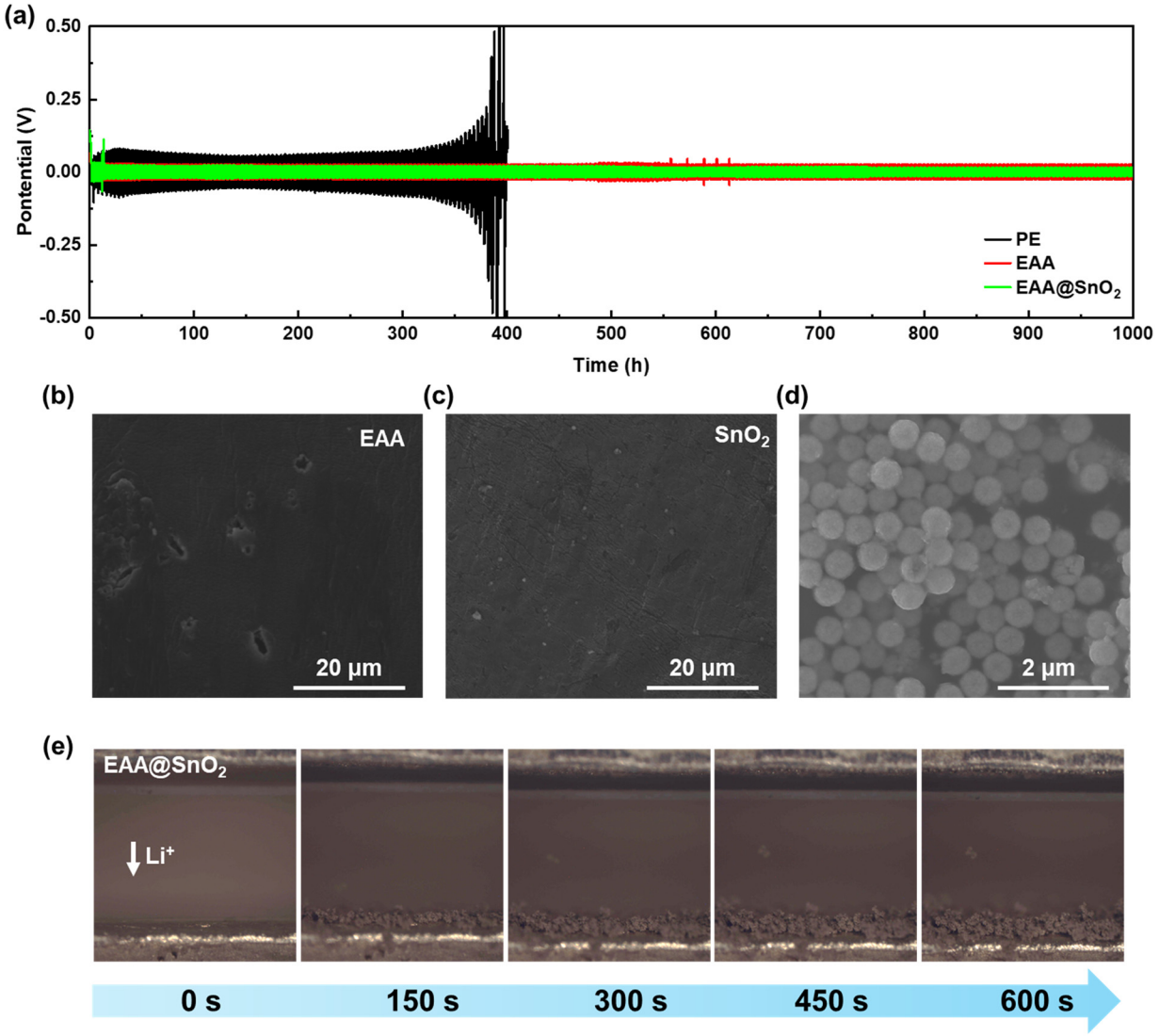


**Fig. 4** (a) Voltage–time curves of Li|PE|Li, Li|EAA|Li and Li|EAA@$SnO_2$|Li symmetric cells at current densities of 0.5 mA $cm^{-2}$ and 1 mA h $cm^{-2}$. The SEM images of the Li anode facing the (b) EAA side and (c) $SnO_2$ side after cycling for 100 h. (d) The SEM image of the EAA@$SnO_2$ separator facing the $SnO_2$ side after cycling. (e) The morphology evolution of the *in situ* Li||Li symmetric cells with the EAA@$SnO_2$ separator at a current of 3 mA.

to reflect the redox ability of the EAA@$SnO_2$-based cell. As shown in Fig. S10,† the redox peaks of 3.55 V and 3.33 V refer to the reaction of the LFP electrode, illustrating the cycling reactivity of the cells. Moreover, the intensity of redox peaks is increased with cycling, representing the activation process of hollow $SnO_2$ nanospheres transforming into $Li_xSn$ alloys. As displayed in Fig. 5a, the initial capacity of the LFP|EAA@$SnO_2$|Li cell reaches 151.0 mA h $g^{-1}$ at 1C, significantly exceeding the capacities of the EAA (142.4 mA h $g^{-1}$) and PE (141.3 mA h $g^{-1}$) separator-assembled cells. In particular, the LFP|EAA@$SnO_2$|Li cell demonstrates an outstanding capacity retention of 54.83% after 1000 cycles at 1C, which is higher than that of the EAA separator (45.44%) and nearly 2 times higher than that of the PE separator (30.36%). The rate performances were also tested for these separator-assembled LFP||Li cells. As shown in Fig. 5b and c, the rate capacities of the LFP|EAA@$SnO_2$|Li cell are 153.4, 144.2, 129.3, 118.2, 110.3 and 103.2 mA h $g^{-1}$ at 0.5, 1, 2, 3, 4 and 5C, respectively. Moreover, the LFP|EAA@$SnO_2$|Li cell shows a characteristic charge–discharge profile, with cell polarization progressively increasing as the current density is elevated. Here, the impact of the $SnO_2$ layer thickness was further evaluated by preparing EAA@$SnO_2$ separators with an increased thickness of 2 μm (EAA@$SnO_2$-TH). As shown in Fig. S11,† the cell with the EAA@$SnO_2$-TH separator exhibits an inferior rate capacity compared to the EAA@$SnO_2$ separator, indicating that the increased $SnO_2$ thickness elongates the ion transport path and thereby compromise the battery performance. Notably, the EAA@$SnO_2$-based LFP||Li cell demonstrates a significantly higher capacity at 5C compared to EAA and PE-based cells, underscoring its superior high-rate performance. This is attributed to the ability of $SnO_2$ to enhance electron transport on the anode, while the generated $Li_xSn$ alloys effectively adjust the electric field distribution and reduce the interfacial

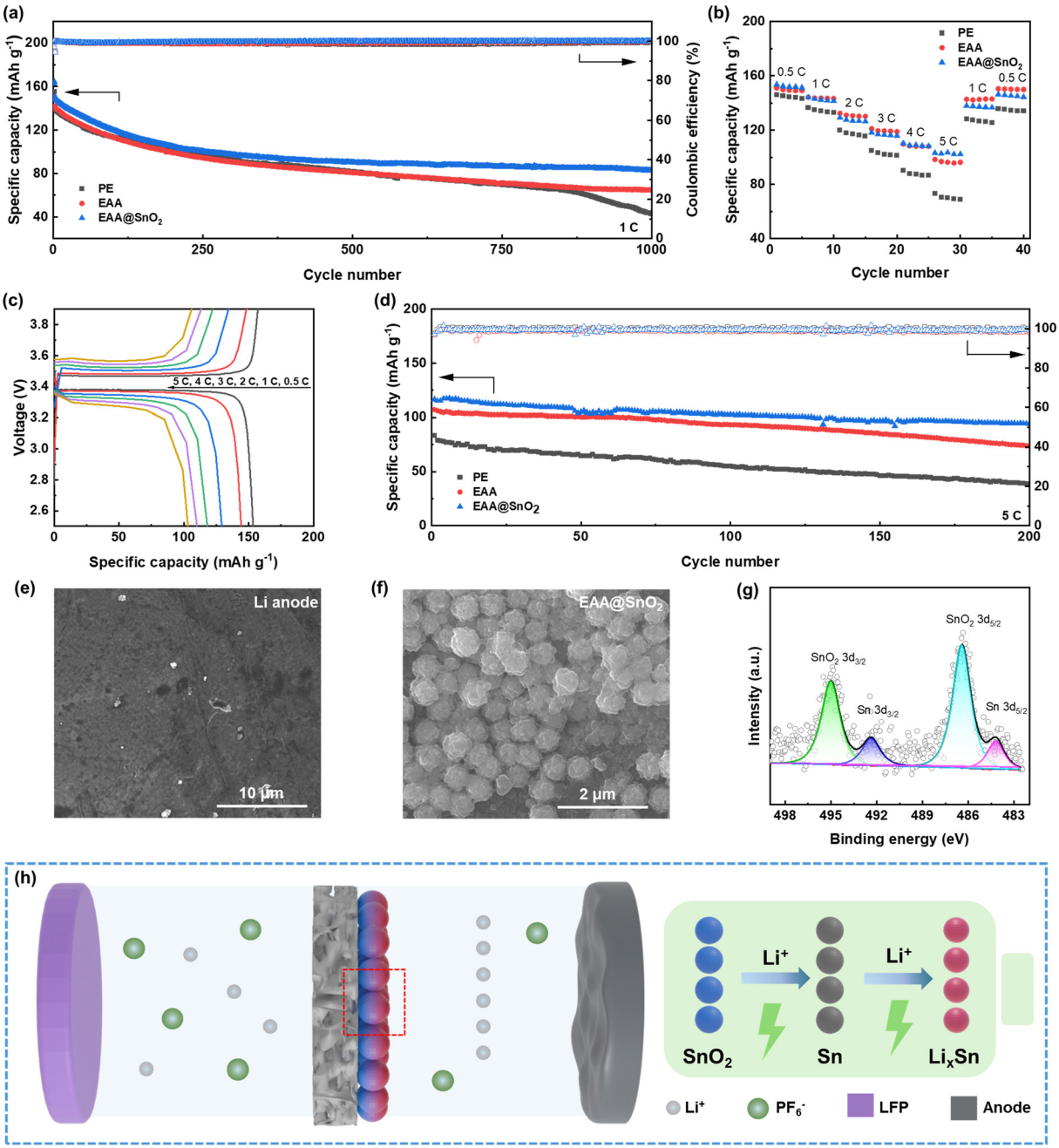


**Fig. 5** (a) The long-term cycling performance of PE, EAA and EAA@$SnO_2$ assembled LFP||Li cells at 1C. (b) The rate capacity of LFP|PE|Li, LFP|EAA|Li and LFP|EAA@$SnO_2$|Li cells from 0.5C to 5C. (c) The charge–discharge profiles of LFP|EAA@$SnO_2$|Li cells from 0.5C to 5C. (d) The long-term cycling performance of PE, EAA and EAA@$SnO_2$ assembled LFP||Li cells at 5C. The SEM images of the (e) Li anode and (f) EAA@$SnO_2$ separator after cycling for 100 cycles at 1C in LFP|EAA@$SnO_2$|Li cells. (g) The XPS spectrum of Sn 3d for EAA@$SnO_2$ separators after cycling for 100 cycles at 1C in LFP|EAA@$SnO_2$|Li cells. (h) The mechanism scheme of EAA@$SnO_2$ separators.

impedance.[39] Thus, the long-term cycling performance at a high rate of 5C was evaluated. As illustrated in Fig. 5d, the capacity of the EAA@$SnO_2$-based cell is 116.6 mA h $g^{-1}$, significantly better than those of EAA and PE-based cells. Notably, the capacity retention of EAA@$SnO_2$ reaches 80.96% after 200 cycles, almost double that of the PE separator (46.46%), highlighting the superior high-rate performance of EAA@$SnO_2$. Similarly, the conductive $Li_xSn$ alloys formed on the separator enhances $Li^+$ transport, facilitating the rapid and uniform $Li^+$ deposition, which effectively supports high-rate performance. Cells with a high LFP loading of 11.25 mg $cm^{-2}$ were tested to evaluate the performance of the EAA@$SnO_2$ separators. As shown in Fig. S12,† the EAA@$SnO_2$-based cell operates steadily for over 60 cycles at 1C with a steady coulombic efficiency. In contrast, the cells using EAA and PE separators exhibit rapid capacity decay

after 25 and 40 cycles, accompanied by fluctuations in Coulombic efficiency, highlighting the excellent dendrite inhibiting capability of the EAA@$SnO_2$ separator.

To assess dendrite suppression of the separator and confirm the structural stability of hollow $SnO_2$ nanospheres on the EAA@$SnO_2$ separator, SEM analysis was employed to investigate the surface morphologies of the anode and separator after 100 cycles at 1C. As shown in Fig. 5e, a uniform Li deposition is observed on the anode, illustrating the homogenous $Li^+$ flux from the $Li_xSn$ alloys. In addition, a dense and thin Li deposition is observed from the LFP|EAA@$SnO_2$|Li cell in the cross-section SEM images of the Li anode (Fig. S13a†). However, a dense but thick Li deposition is observed from the LFP|EAA|Li cell while the LFP|PE|Li cell exhibits a loose Li deposition (Fig. S13b and c†), further emphasizing the superior dendrite suppression of the EAA@$SnO_2$ separator. Notably, the hollow $SnO_2$ nanospheres retain their morphology from the SEM image of the cycled EAA@$SnO_2$ separator (Fig. 5f), indicating that the hollow structure provides sufficient space to accommodate volume expansion. Moreover, as displayed in the EDX mapping in Fig. S14,† the distribution of F and P from the electrolyte coincides with that of $SnO_2$ on the cycled separator, suggesting that the hollow $SnO_2$ nanospheres retain a significant amount of electrolyte, which contributes to their hollow structure and enhances the battery performance. XPS was conducted to confirm the reactions involved in the transformation of $SnO_2$ into $Li_xSn$ alloys. As shown in Fig. 5g, peaks of Sn in Sn 3d XPS are observed in addition to $SnO_2$, indicating the reaction between $SnO_2$ and Li. Besides, the presence of $Li_2O$ peaks in the Li 1s XPS spectrum further supports this transformation (Fig. S15†). The XRD pattern of the cycled EAA@$SnO_2$ separator also exhibits two distinct diffraction peaks at approximately 30° and 32° (Fig. S16†), which can be indexed to $Li_xSn$ alloys ($Li_{22}Sn_5$ PDF: 00-018-0753), confirming the generation of $Li_xSn$ alloys during cycling. In addition, XPS was also performed on the Li anode to investigate the effect of $SnO_2$ on SEI formation. As shown in Fig. S17,† the absence of Sn signals in XPS indicates that $SnO_2$ does not participate in the formation of the SEI. This also illustrates the excellent structural stability of $SnO_2$ during cycling. Furthermore, thanks to the high lithiophilicity of $Li_xSn$ alloys, the charge transfer impedance ($R_{ct}$) of the EAA@$SnO_2$-based cell decreases significantly to 38 Ω from 79 Ω after 100 cycles at 1C, whereas the $R_{ct}$ of EAA and PE increases after cycling (Fig. S18†).

Therefore, the EAA matrix and $SnO_2$ coating work synergistically to enhance the ability of separators to suppress the dendrite formation. As shown in Fig. 5h, the incorporation of hollow $SnO_2$ nanospheres, subsequently converted to $Li_xSn$ alloys through a two-step reaction which are listed in eqn (3) and (4), leads to the formation of lithiophilic $Li_xSn$ alloys. $Li_xSn$ alloys enhance ionic rectification and generate a uniform electric field between the anode and separator, which facilitates a homogeneous $Li^+$ flux. Meanwhile, the EAA increases the $t_{Li^+}$ with carboxyl groups and promotes the desolvation of $LiPF_6$, which leads to an increase in free $Li^+$ and enhances their transport. Moreover, the structural modification of hollow $SnO_2$ nanospheres significantly promotes $Li^+$ transport as well and effectively regulates $Li^+$ flux, ultimately resulting in a stable, dendrite-free anode and markedly improved high-rate performance.

$$SnO_2 + 4Li^+ + 4e^- \rightarrow Sn + 2Li_2O \quad (3)$$

$$xLi^+ + xe^- + Sn \rightarrow Li_xSn(0 \le x \le 4.4) \quad (4)$$

## Conclusions

In summary, lithiophilic hollow $SnO_2$ nanospheres are coated on the EAA separator, improving the electrolyte uptake and wettability. Benefiting from the synergistic effects of carboxyl groups in the EAA matrix and the $SnO_2$ coating layer, the EAA@$SnO_2$ separator achieves a $t_{Li^+}$ of 0.74. The hollow $SnO_2$ nanospheres regulate the $Li^+$ flux, benefiting the formation of a flat SEI. Furthermore, during cell operation, the $SnO_2$ transforms into $Li_xSn$ alloys through a two-step reaction. The lithiophilic nature of the generated $Li_xSn$ alloys enhances $Li^+$ transport and improves the high-rate performance of assembled cells. As a result, the EAA@$SnO_2$-based cells deliver a stable Li plating/tripping of over 1000 h with a low voltage hysteresis of 17 mV at 0.5 mA $cm^{-2}$. The LFP|EAA@$SnO_2$|Li cell achieves a high discharge capacity of 116.6 mA h $g^{-1}$ at 5C, with a capacity retention of 80.96% after 200 cycles. These findings present a novel metallic coating material for separators, which enables high performance and dendrite-free LMBs.

## Data availability

The data that support the findings of this study are available from the corresponding author upon reasonable request.

## Author contributions

Y. C. and H. N. conceived the idea and designed the EAA@$SnO_2$ separators. Y. C. and H. N. have designed the experiments. Y. C., X. Z., Y. Y. and X. W. have conducted the experiments. Y. C. has drafted the article, and all authors contributed to the final manuscript.

## Conflicts of interest

There are no conflicts to declare.

## Acknowledgements

The authors acknowledge financial support from the Major International (Regional) Joint Cooperation Research Project of the National Natural Science Foundation of China (52020105012), the Young Scientists Fund of National Natural Science Foundation of China (52303084), and the Young

Scientists Fund of Natural Science Foundation of Hubei Province (2023AFB220) and analytical and testing assistance from the Analysis and Testing Center of HUST.

## Notes and references

1 J. Feng, J. Wang, Q. Gu, P. Li, H. Xu, Y. Deng and P. Gao, *Adv. Funct. Mater.*, 2025, **35**, 2412287.
2 Y. Mu, Y. Chu, Y. Shi, C. Huang, L. Yang, Q. Zhang, C. Li, Y. Feng, Y. Zhou, M. Han, T. Zhao and L. Zeng, *Adv. Energy Mater.*, 2024, **14**, 2400725.
3 Q. Zhang, B. Hou, X. Wu, X. Li, Z. Guo, J. Liu, D. Cao, X. Huang, J. Duan, D. Mo, J. Liu and H. Yao, *Adv. Energy Mater.*, 2024, **14**, 2401377.
4 S. Zheng, S. Bi, Y. Fu, Y. Wu, M. Liu, Q. Xu and G. Zeng, *Adv. Mater.*, 2024, **36**, 2313076.
5 X. Wu, S. Zhang, X. Xu, F. Wen, H. Wang, H. Chen, X. Fan and N. Huang, *Angew. Chem.*, 2024, **136**, e202319355.
6 W. Tang, T. Zhao, K. Wang, T. Yu, R. Lv, L. Li, F. Wu and R. Chen, *Adv. Funct. Mater.*, 2024, **34**, 2314045.
7 W. Xin, J. Xiao, J. Li, L. Zhang, H. Peng, Z. Yan and Z. Zhu, *Energy Storage Mater.*, 2023, **56**, 76–86.
8 L. Cao, M. Chu, Y. Li, X. Xu, Y. Qiu, Y. Dai, C. Sun, Z.-X. Huang, X.-L. Wu and H. Geng, *Adv. Mater.*, 2024, **36**, 2406034.
9 J. Lee, S. H. Jeong, J. S. Nam, M. Sagong, J. Ahn, H. Lim and I.-D. Kim, *EcoMat*, 2023, **5**, e12416.
10 B. Ma, H. Zhang, R. Li, S. Zhang, L. Chen, T. Zhou, J. Wang, R. Zhang, S. Ding, X. Xiao, T. Deng, L. Chen and X. Fan, *Nat. Chem.*, 2024, **16**, 1427–1435.
11 Y. Li, Q. Qu, L. Lv, J. Shao and H. Zheng, *Adv. Funct. Mater.*, 2024, **34**, 2314100.
12 T. Wang, B. Chen, C. Liu, T. Li and X. Liu, *Angew. Chem., Int. Ed.*, 2024, **63**, e202400960.
13 M. Yao, Q. Ruan, S. Pan, H. Zhang and S. Zhang, *Adv. Energy Mater.*, 2023, **13**, 2203640.
14 A. Du, H. Lu, S. Liu, S. Chen, Z. Chen, W. Li, J. Song, Q.-H. Yang and C. Yang, *Adv. Energy Mater.*, 2024, **14**, 2400808.
15 D. Kang, S. Sardar, R. Zhang, H. Noam, J. Chen, L. Ma, W. Liang, C. Shi and J. P. Lemmon, *Energy Storage Mater.*, 2020, **27**, 69–77.
16 H. Song, J. Lee, M. Sagong, J. Jeon, Y. Han, J. Kim, H.-G. Jung, J.-S. Yu, J. Lee and I.-D. Kim, *Adv. Mater.*, 2024, **36**, 2407381.
17 H. Jia, C. Zeng, H.-S. Lim, A. Simmons, Y. Zhang, M. H. Weber, M. H. Engelhard, P. Gao, C. Niu, Z. Xu, J.-G. Zhang and W. Xu, *Adv. Mater.*, 2024, **36**, 2311312.
18 Y. Ji, L. Dong, J. Liu, H. Xie, S. Zhong, C. Yang, J. Han and W. He, *Energy Environ. Sci.*, 2024, **17**, 4078–4089.
19 Y. Ji, C. Yang, J. Han and W. He, *Adv. Energy Mater.*, 2024, **14**, 2402329.
20 X. Lin, R. Baranwal, G. Ren and Z. Fan, *Chem. Eng. J.*, 2024, **500**, 157192.
21 K. Wang, T. Zhao, R. Lv, W. Tang, T. Yu, G. Chen, L. Li, F. Wu and R. Chen, *Adv. Energy Mater.*, 2024, **14**, 2401281.
22 L. Zuo, Q. Ma, P. Xiao, Q. Guo, W. Xie, D. Lu, X. Yun, C. Zheng and Y. Chen, *Adv. Mater.*, 2024, **36**, 2311529.
23 A. Jung, M. J. Lee, S. W. Lee, J. Cho, J. G. Son and B. Yeom, *Small*, 2022, **18**, 2205355.
24 X. Wang, Y. Wen, Y. Wang, Y. Chen, L. Yang, C. Guo, H. Nie, X. Zhou and X. Xie, *J. Power Sources*, 2024, **615**, 235126.
25 Y. Liu, X. Tao, Y. Wang, C. Jiang, C. Ma, O. Sheng, G. Lu and X. W. Lou, *Science*, 2022, **375**, 739–745.
26 Z. Zhang, J. Wang, H. Qin, B. Zhang, H. Lin, W. Zheng, D. Wang, X. Ji and X. Ou, *ACS Nano*, 2024, **18**, 2250–2260.
27 D. Li, Y. Ouyang, Y. Xiao, Y. Xie, Q. Zeng, S. Yu, C. Zheng, Q. Zhang and S. Huang, *Adv. Funct. Mater.*, 2024, **34**, 2314296.
28 L. Zhou, H. Pan, G. Yin, Y. Xiang, P. Tan, X. Li, Y. Jiang, M. Xu and X. Zhang, *Adv. Funct. Mater.*, 2024, **34**, 2314246.
29 S. A. Han, H. Qutaish, J.-W. Lee, M.-S. Park and J. H. Kim, *EcoMat*, 2023, **5**, e12283.
30 G. Yu, Y. Cui, S. Lin, R. Liu, S. Liu, Y. Zhu and D. Wu, *Adv. Funct. Mater.*, 2024, **34**, 2314935.
31 S. Yao, Y. Yang, Z. Liang, J. Chen, J. Ding, F. Li, J. Liu, L. Xi, M. Zhu and J. Liu, *Adv. Funct. Mater.*, 2023, **33**, 2212466.
32 M. Du, Z. He, Y. Zhang, Y. Cai and Q. Zheng, *Adv. Energy Mater.*, 2025, 2403674.
33 X. Li, K. Liu, N. Dong, B. Liu, G. Tian, S. Qi and D. Wu, *Chem. Eng. J.*, 2024, **481**, 148525.
34 X. Zeng, Y. Chen, H. Nie, Y. Yang, J. Chen, H. Pei, X. Wang, Y. Yang, J. Pang, X. Zhou, G. Wang and X. Xie, *Small*, 2025, **21**, 2411626.
35 D. Li, D. Shi, K. Feng, X. Li and H. Zhang, *J. Membr. Sci.*, 2017, **530**, 125–131.
36 Q. Zhao, R. Zhou, C. Wang, J. Kang, Q. Zhang, J. Liu, Y. Jin, H. Wang, Z. Zheng and L. Guo, *Adv. Funct. Mater.*, 2022, **32**, 2112711.
37 Y. Chen, P. Mickel, H. Pei, Y. Wen, X. Guan, Y. Wang, X. Wang, O. A. Mhtachem, C. Zhang, H. Nie, X. Zhou, P. Kral and X. Xie, *ACS Appl. Mater. Interfaces*, 2023, **15**, 18333–18342.
38 Y. Liu, S. Xiong, J. Wang, X. Jiao, S. Li, C. Zhang, Z. Song and J. Song, *Energy Storage Mater.*, 2019, **19**, 24–30.
39 Y. Ma, F. Wu, N. Chen, Y. Ma, C. Yang, Y. Shang, H. Liu, L. Li and R. Chen, *Chem. Sci.*, 2022, **13**, 9277–9284.
40 H. Lee, X. Ren, C. Niu, L. Yu, M. H. Engelhard, I. Cho, M.-H. Ryou, H. S. Jin, H.-T. Kim, J. Liu, W. Xu and J.-G. Zhang, *Adv. Funct. Mater.*, 2017, **27**, 1704391.
41 C. Yue, S. Sun, M. Jang, E. Park, B. Son, H. Son, Z. Liu, D. Wang, U. Paik and T. Song, *Electrochim. Acta*, 2021, **370**, 137703.
42 H. G. Nam, J. Y. Park, J. M. Yuk and S. M. Han, *Energy Storage Mater.*, 2022, **45**, 101–109.
43 Y. Xiang, Z. Wang, W. Qiu, Z. Guo, D. Liu, D. Qu, Z. Xie, H. Tang and J. Li, *J. Membr. Sci.*, 2018, **563**, 380–387.
44 N. Hu, X. Lv, Y. Dai, L. Fan, D. Xiong and X. Li, *ACS Appl. Mater. Interfaces*, 2018, **10**, 18665–18674.
45 X.-D. Zhu, C. Han, J. Zhang, W. Mi, Y. Qin, J. Gao, J. Wu, J.-J. Zou, X. Yang, Y.-C. Zhang and G. Wu, *EcoMat*, 2023, **5**, e12291.
46 J. Kim, S. Lee, J. Kim, J. Park, H. Lee, J. Kwon, S. Sun, J. Choi, U. Paik and T. Song, *Carbon Energy*, 2024, **6**, e610.
47 D. Ding, H. Tao, X. Fan, X. Yang and L. Fan, *Adv. Funct. Mater.*, 2024, **34**, 2401457.
48 F. Liang, H. Dong, Z. Ji, W. Zhang, H. Zhang, C. Cao, H. Li, H. Liu, K.-Q. Zhang, Y. Lai, Y. Tang and M. Ge, *Sci. China Mater.*, 2023, **66**, 1736–1746.